



Full Length Article

In silico actuation performance investigation of dielectric elastomers with TPMS geometries

Mohammad Ali Safaei^a, Mostafa Baghani^{a, **}, Majid Baniassadi^a, Mahdi Bodaghi^{b, *} ^a School of Mechanical Engineering, College of Engineering, University of Tehran, Tehran, Iran^b Department of Engineering, School of Science and Technology, Nottingham Trent University, Nottingham, NG11 8NS, UK

ARTICLE INFO

Keywords:

Dielectric elastomer actuators
Architected materials
Triply periodic minimal surface
Microstructural design
Two-phase materials

ABSTRACT

Dielectric Elastomer Actuators (DEAs) are highly efficient soft actuators widely used in soft robotics and artificial muscles due to their superior actuation capabilities. Introducing two-phase structures to DEAs offers potential benefits, particularly in reducing operational voltages. However, this approach poses significant challenges due to both physical and numerical constraints. This study investigates the distinctive actuation performance of two-phase microstructure DEAs, designed using a class of architected materials known as Triply Periodic Minimal Surfaces (TPMS), and compares them with Random Heterogeneous Microstructures. Six well-known TPMS geometries, including Gyroid, Schwarz-P, and IWP structures, are employed. In addition to actuation performance, localized electric fields and blocking forces are analyzed for all microstructures to provide a comprehensive understanding of their behavior. The quasi-static, fully coupled governing equations of DEAs are implemented in ABAQUS software using a reliable in-silico FEM approach. The results reveal that DEAs based on TPMS geometries exhibit intrinsic advantages over their random counterparts in terms of actuation performance. Notably, the microstructure named Octo demonstrates the highest improvement, showing a 9.9% increase in actuation performance compared to Random Microstructures. However, this trend is reversed with respect to blocking forces, where Random Microstructures exhibit higher values. The analysis of localized electric fields indicates that both TPMS- and Random-based microstructures have the potential to offer relatively low localized fields. These findings represent a preliminary step toward the development of multi-phase DEA composites with architected geometries.

1. Introduction

Recent advancements in robotics have underscored the importance of flexibility, safe interaction, and adept navigation in confined spaces, thereby elevating the role of soft actuators (Gu et al., 2017), (Zhang et al., 2023). These actuators are intelligent materials that respond to a variety of stimuli, such as temperature changes, chemical interactions, etc. (Safavi et al., 2023), (Askari-Sedeh and Baghani, 2023), (Ahangari et al., 2024), (Enferadi et al., 2024). Among these materials, dielectric elastomer actuators (DEAs) have emerged as particularly promising. These remarkable devices exploit electrostatic forces to enable reconfigurable motion within their structures. DEAs provide substantial actuation capabilities, cost-effectiveness, noise-free operation, fast response, and high specific energy density. These unique features make DEAs excellent candidates for applications such as artificial muscles, soft

robotics, tactile displays, and energy harvesting (Duduta et al., 2019), (Feng et al., 2024), (Ji et al., 2021), (Moretti et al., 2020), (Yuan et al., 2024) (see Fig. 1a). The most fundamental DEA consists of a rectangular elastomer film coated with compliant electrodes on opposing sides. When an electrical potential is applied to these electrodes, an electrostatic pressure develops, causing the structure to contract in thickness. Simultaneously, this contraction induces lateral expansion, which constitutes the actuation mode of the DEA (see Fig. 1b).

Developing novel DEAs involves addressing several critical challenges. On one hand, achieving optimal DEA performance—high actuation strain at low voltages—requires designing materials with both high permittivity and compliance while maintaining a thin structure. Additionally, mitigating dominant failure modes such as electromechanical instability (EMI) and electrical breakdown is essential, whether through structural improvements or material modifications. Numerous

* Corresponding author.

** Corresponding author.

E-mail addresses: baghani@ut.ac.ir (M. Baghani), mahdi.bodaghi@ntu.ac.uk (M. Bodaghi).

innovative solutions have been proposed in the literature, including inherently pre-stretched structures (Niu et al., 2013) or materials possessing strain-stiffening effect (Li et al., 2017), tailoring novel composite DEAs (Zhang et al., 2020), (Hu et al., 2014) as well as blend DEAs (Tian et al., 2014), and chemically modifying conventional DEA materials (Racles et al., 2013). For comprehensive details, interested readers can refer to (Romasanta et al., 2015), (Madsen et al., 2016). Apart from experimental studies, the efficient design of DEAs requires investigating the large deformation phenomena that occur under electromechanical loading. Various constitutive models have been proposed, including linear elastic models that exhibit high error rates at large strains (Pelrine et al., 2000), (Pelrine et al., 2002), and more reliable models based on finite strain theory, which effectively capture DEA behavior (Suo, 2010), (Behera et al., 2021). Additionally, efforts have been made to propose analytical models that estimate the onset of instability in DEAs (Zhou et al., 2008), (Bahreman et al., 2022). These models prove valuable for simple geometries such as rectangular, tabular (An et al., 2015), (Liu et al., 2022) and spherical ones (Xing and Yong, 2021). Recent advancements have led to the development of more practical DEAs with complex geometries (Hajiesmaili et al., 2019), (Hajiesmaili and Clarke, 2019), (Hajiesmaili et al., 2024), (Liu et al., 2020). Analyzing these advancements has become increasingly challenging due to the need to solve coupled multi-physics governing equations on complex geometries. The Finite Element Method (FEM), a powerful tool for tackling complex problems in solid mechanics (Shen et al., 2024), (Long et al., 2023), is commonly employed to address this challenge. In this regard, reliable finite element models have been developed in recent studies (Hajiesmaili and Clarke, 2021).

Microstructure DEAs can be customized to enhance their performance and practicality. To achieve this, pre-designed architectures can be applied to these materials, incorporating specific desired performance characteristics. Among the various available architectures, Triply Periodic Minimal Surfaces (TPMS), as a class of bio-inspired meta-materials, stand out as a promising class of cellular structures. TPMS

structures are mathematically defined surfaces with zero mean curvature at each point, resulting in smooth phase boundaries (Feng et al., 2022). These geometries can be frequently found in natural examples (Gan et al., 2016), (Han and Che, 2018) (see Fig. 1c). High modulus, high surface-to-volume ratio and fluid permeability make TPMS-based structures excellent candidates for energy absorbers, heat exchangers, bone scaffolds and other applications (Sang et al., 2023), (Xi et al., 2023), (Li et al., 2020), (Kapfer et al., 2011), (Werner et al., 2018), (Shirzad et al., 2023), (Tian et al., 2023) (see Fig. 1d). Thus far, a significant number of these experiments have focused on TPMS-based hard materials (Maskery et al., 2017), (Lu et al., 2021). As a result, many constitutive models proposed in the literature rely on the linear elastic assumption (Khaleghi et al., 2023), (Khaleghi et al., 2021). Although a few valuable studies have been conducted on smart materials with TPMS geometries (Sadeghi et al., 2023), (Imanian et al., 2023), (Chen et al., 2022), (Roudbarian et al., 2022), (Singh et al., 2022), these efforts are still in their early stages. This is mainly due to the complex multi-physics behavior governing smart materials, which makes computational analysis challenging, especially for structures with complex geometries. As a result, a significant gap remains in the study of soft actuators with complex geometries. However, the unique characteristics of TPMS, as discussed earlier, provide the foundation for the present work, which aims to explore this gap with the expectation of yielding valuable insights.

This study explores the potential benefits of using TPMS-based two-phase microstructures in DEAs (referred to as P-DEAs), particularly for reducing operating voltages. To highlight the distinctive actuation behaviors of these microstructures, the study compares them to fully Random and anisotropic Random Heterogeneous Microstructures (referred to as R-DEAs). The research also examines localized electric fields and blocking forces in these microstructures to provide a comprehensive assessment. In Section 2, the TPMS-based microstructures used in this study, including well-known geometries such as Schwarz-P and Gyroid, as well as two types of Random Heterogeneous

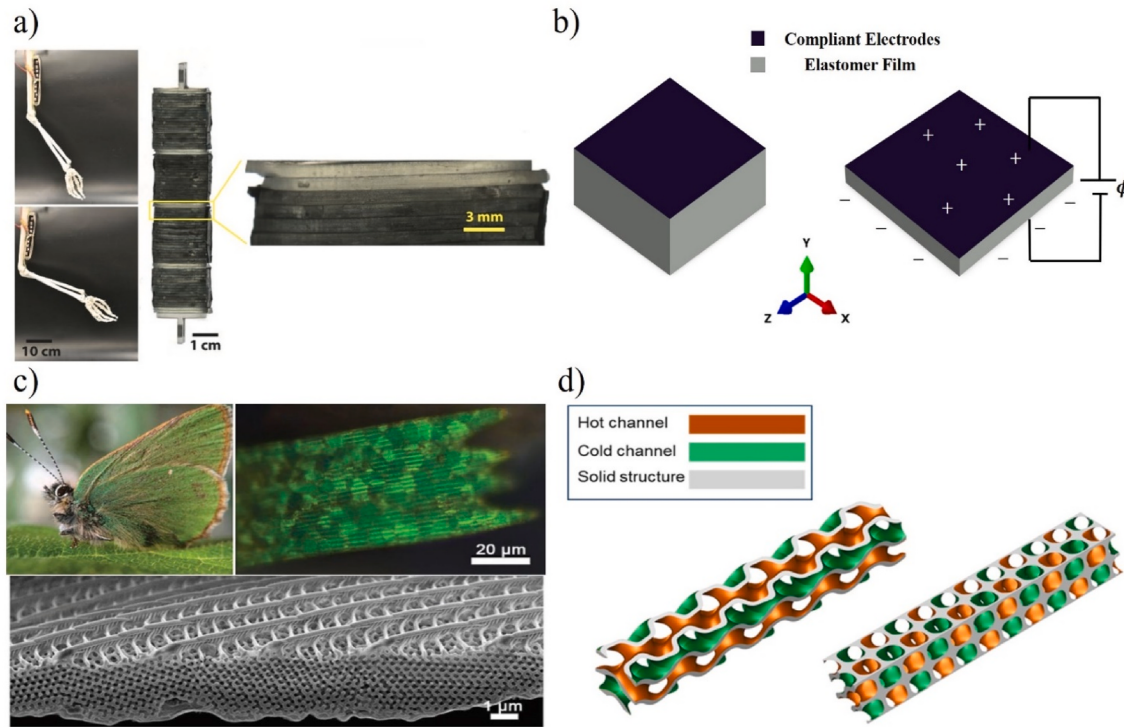


Fig. 1. a) Utilization of multi-layered DEAs as artificial muscles in a robotic arm (Duduta et al., 2019). b) Electromechanical performance of DEAs under the voltage (ϕ). c) Photograph of a butterfly, alongside microscopic and SEM images of its wings at different scales (Corkery and Tyrode, 2017). d) Heat exchangers inspired by Gyroid and Schwarz-D geometries (Li et al., 2020).

Microstructures, are introduced. Additionally, the previously-developed governing equations are described within a continuum mechanics framework to model their electromechanical actuation. The finite element method protocol for implementing the discretized equations in the ABAQUS commercial software is also explained. In Section 3, the results of the analyses are presented and discussed in relation to the aforementioned criteria, with the best- and worst-performing microstructures highlighted. In Section 4, the study's most significant findings are summarized, and recommendations for future work are provided.

2. Methodology

Dielectric Elastomer Actuators (DEAs) undergo significant deformations under electromechanical loading. Hyperelasticity theory provides a practical framework to describe this behavior. In this section, the quasi-static, fully-coupled governing equations of DEAs are derived based on hyperelasticity theory, then discretized into a standard FEM format. Next, the TPMS structures used in this study are introduced, along with an overview of their properties. Finally, the protocol for implementing the standard FEM form of the equations in ABAQUS, as well as other aspects of the FEM analysis of the microstructure DEAs problem, are outlined.

2.1. Governing equations

2.1.1. Differential form

In the context of DEAs subjected to electromechanical loading, a system of coupled equations, addressing mechanical and electrical aspects of the problem, governs the behavior. These governing equations, expressed in differential form, are as follows:

$$\begin{aligned} \frac{\partial}{\partial x_i} (\sigma_{ij} + \sigma_{ij}^{Maxwell}) &= 0, \quad j = 1, 2, 3 \\ \frac{\partial D_i}{\partial x_i} &= q \end{aligned} \quad (1)$$

where \vec{x} , σ , $\sigma^{Maxwell}$, \vec{D} and q represent the current coordinates vector, Cauchy stress tensor, Maxwell stress tensor, electric displacement field, and the density of free charges, respectively. The first equation depicts the balance of linear momentum, wherein the total stress tensor is decomposed into the Cauchy stress tensor and the electric field-induced Maxwell stress tensor. It is important to note that in the subsequent paragraph, each stress tensor is introduced separately. The second equation corresponds to Gauss's law, which establishes a relationship between the distribution of electric charges and the resulting electric displacement within the volume. By definition, the electric displacement is the sum of the electric field scaled by the vacuum electric permittivity ($8.85 \times 10^{-12} \frac{F}{m}$) and the polarization density of the dielectric: $\vec{D} = \epsilon_0 \vec{E} + \vec{P}$. Assuming the dielectrics in this study behave similarly to liquid-like dielectrics, where the material polarization is proportional to the applied electric field ($\vec{P} \propto \vec{E}$), and the electric displacement field is proportional to the applied electric field with the material permittivity, ($\epsilon = \epsilon_0 \epsilon_r$, where ϵ_r is the relative permittivity specific to the material), the relationship for the electric displacement reduces to: $\vec{D} = \epsilon \vec{E}$.

The Cauchy stress tensor, σ , serves as the initial component of the total stress within the system and is defined by hyper-elasticity theory. Within this theoretical framework, a Helmholtz free energy function is considered for each system, capturing its response to external forces. This energy function characterizes the mechanical energy of the system using various strain tensors, including the left Cauchy-Green strain tensor. Specifically, it can be expressed as $\mathbf{b} = \mathbf{FF}^T$, where \mathbf{F} represents the deformation gradient tensor that relates the current and initial states of the system. Various constitutive models have been developed in the literature for the Helmholtz free energy function of DEAs, including Neo-Hookean (Firoozan et al., 2024), Mooney-Rivlin (Ahmadi and Asgari,

2020), etc. Given the relatively small stretches in this study ($\lambda < 3$), the Neo-Hookean Helmholtz free energy function is accurate and has been adopted. The Neo-Hookean Helmholtz free energy function, expressed in terms of principal stretches, is given by:

$$\psi(\bar{I}_1, J) = \frac{\mu}{2}(\bar{I}_1 - 3) + \frac{\kappa}{2}(J - 1)^2 \quad (2)$$

with μ and κ representing the shear modulus and bulk modulus, respectively. The expression ($\bar{I}_1 = I_1/I_3^{1/3}$) denotes the isochoric component of the first invariant of the Cauchy-Green deformation tensor (i.e., $I_1 = \text{trace}(\mathbf{b}) = \lambda_1^2 + \lambda_2^2 + \lambda_3^2$). Additionally, J represents the determinant of the deformation gradient tensor and is equal to the square root of the third invariant of the Cauchy-Green deformation tensor (i.e., $J = \sqrt{I_3} = \sqrt{\lambda_1^2 \lambda_2^2 \lambda_3^2} = \lambda_1 \lambda_2 \lambda_3$). The first term in equation (2) corresponds to the isochoric deformations within the system, while the second term accounts for volume changes during deformation. Knowing Poisson's ratio (ν) and the shear modulus (μ) of the material as material parameters, the bulk modulus (κ) can be evaluated using the following equation: $\kappa = \frac{2\mu(1+\nu)}{3(1-2\nu)}$. The material parameters used in this study are presented in Table 2.

By taking the derivatives of the Helmholtz free energy function (Eq. (2)), the Cauchy stress tensor, σ , can be described as:

$$\sigma = \left(\frac{\mu}{J^{5/3}} \right) \mathbf{b} + \left(-\frac{\mu}{3J} \bar{I}_1 + \kappa(J - 1) \right) \mathbf{I} \quad (3)$$

in which \mathbf{I} is the identity tensor. As the second part of the total stress tensor, Maxwell stress tensor, $\sigma_{ij}^{Maxwell}$, describes the interaction between electromagnetic forces and mechanical momentum. In the absence of magnetic fields, $\sigma_{ij}^{Maxwell}$ simplifies to:

$$\sigma_{ij}^{Maxwell} = \epsilon \left(E_i E_j - \frac{1}{2} \delta_{ij} E_k E_k \right) \quad (4)$$

wherein δ is the Kronecker delta.

2.1.2. Discretization

For the finite element implementation of the governing equations (i.e., Eq. (1)), they must first be transformed into a system of algebraic equations. This transformation, known as discretization, can be achieved using weighted residual methods. A similar procedure has been carried out in previous studies, and this study leverages that approach to perform a reliable FEM analysis. The discretization of the governing equations proceeds in the following manner.

In this specific case, the Ritz method is employed to derive the weak form of the governing equations. By combining the Ritz method with the Gaussian quadrature integration scheme, the residuals of the governing equations are discretized into a set of algebraic equations with respect to the displacement (u) and the voltage (φ), as described below:

$$\begin{cases} R_{u_j}^A \\ R_{\varphi}^A \end{cases} = \begin{cases} \sum_{n_G} \left(-\sigma_{ij} \frac{\partial N^A}{\partial x_i} + b_j N^A \right) w_{n_G} \det \frac{\partial \mathbf{x}_p}{\partial \xi_q} + \sum_{n_G} (T_j N^A) w_{n_G} \det \frac{\partial \mathbf{x}_p}{\partial \xi_q} \\ \sum_{n_G} \left(-D_i \frac{\partial N^A}{\partial x_i} - q N^A \right) w_{n_G} \det \frac{\partial \mathbf{x}_p}{\partial \xi_q} + \sum_{n_G} (q_s N^A) w_{n_G} \det \frac{\partial \mathbf{x}_p}{\partial \xi_q} \end{cases} = \begin{cases} 0 \\ 0 \end{cases} \quad (5)$$

where \rightarrow_b , \rightarrow_T , q_s and w_{n_G} stand for the body forces, surface tractions, the flux of free charge density and integration weights per integration points, respectively. Additionally, $N^A(\xi_1, \xi_2, \xi_3)$ are shape functions expressed in a local coordinate system (ξ_1, ξ_2, ξ_3), and superscript A is the node number. After transformation mapping of the coordinate system (geometrical discretization of the equations) using the same shape

function as the displacement, the system of nonlinear algebraic equations can be solved iteratively using the Newton-Raphson method, accordingly:

$$-\frac{\partial}{\partial u_k^B} \begin{Bmatrix} R_{u_j}^A \\ R_\varphi^A \end{Bmatrix} \delta u_k^B - \frac{\partial}{\partial \varphi^B} \begin{Bmatrix} R_{u_j}^A \\ R_\varphi^A \end{Bmatrix} \delta \varphi^B = \begin{Bmatrix} R_{u_j}^A \\ R_\varphi^A \end{Bmatrix}, j=1, 2, 3, A=1, \dots, N \quad (6)$$

where the superscript B denotes the node numbers after mapping. The above equation can be rewritten in the standard FEM form as follows:

$$\begin{bmatrix} K_{u_j^A u_k^B} & K_{u_j^A \varphi^B} \\ K_{\varphi^A u_k^B} & K_{\varphi^A \varphi^B} \end{bmatrix} \begin{Bmatrix} \delta u_k^B \\ \delta \varphi^B \end{Bmatrix} = \begin{Bmatrix} R_{u_j}^A \\ R_\varphi^A \end{Bmatrix}, j=1, 2, 3, A=1, \dots, N \quad (7)$$

in which K represents the components of the problem's stiffness matrix. For the final step, the Dirichlet and Neumann boundary conditions (BCs) must be specified at the boundary surfaces to fully define the problem. The mathematical representation of these BCs is provided below:

$$\begin{aligned} \vec{x}(\vec{X}) &= \vec{x}_0(\vec{X}) & \forall \vec{X} \in S_u \\ \sigma \cdot n(\vec{X}) &= \sigma_0 \cdot n(\vec{X}) & \forall \vec{X} \in S_\sigma \\ \varphi(\vec{X}) &= \varphi_0(\vec{X}) & \forall \vec{X} \in S_\varphi \\ \vec{E}(\vec{X}) &= \vec{E}_0(\vec{X}) & \forall \vec{X} \in S_E \end{aligned} \quad (8)$$

wherein \vec{x}_0 , σ_0 , φ_0 and \vec{E}_0 represent the displacements, stresses, electric potentials, and electric fields, respectively, specified over the boundary surfaces S_u , S_σ , S_φ and S_E . It is noteworthy that applying \vec{E}_0 on S_E corresponds to the flux of free charge density on that surface.

2.2. Microstructures exploitation

2.2.1. Triply Periodic Minimal Surfaces (TPMS)

The introduction of the first class of bio-inspired TPMS dates back to the 19th century. Mathematician Hermann Schwarz introduced two periodic surfaces, and his student Neovius later introduced a third one, which became known as Neovius geometry. In 1970, Alan Schoen introduced 12 new infinitely connected TPMS structures, including the Gyroid (Schoen, 1970). Since then, numerous other TPMS with unique characteristics have been introduced. Fisher et al. (2023) have compiled the equations for TPMS structures that have appeared in the literature, along with their corresponding properties. The implicit equations of the TPMS structures investigated in the present work are presented as follows:

$$\text{Gyroid : } f(x, y, z) : C_x S_y + C_y S_z + C_z S_x = t \quad (9)$$

$$\text{Schwarz-D : } f(x, y, z) : S_x S_y S_z + S_x C_y C_z + C_x S_y C_z + C_x C_y S_z = t \quad (10)$$

$$\text{IWP : } f(x, y, z) : (C_{2x} + C_{2y} + C_{2z}) - 2(C_x C_y + C_x C_z + C_z C_y) = t \quad (11)$$

$$\text{FRD : } f(x, y, z) : 4C_x C_y C_z - (C_{2x} C_{2y} + C_{2y} C_{2z} + C_{2z} C_{2x}) = t \quad (12)$$

$$\text{Octo : } f(x, y, z) : 0.6(C_x C_y + C_y C_z + C_z C_x) - 0.4(C_x + C_y + C_z) + 0.25 = t \quad (13)$$

$$\text{C(D) : } f(x, y, z) : C_{3x+y} C_z - S_{3x-y} S_z + C_{x+3y} C_z + S_{x-3y} S_z + C_{x-y} C_{3z} - S_{x+y} S_{3z} = t \quad (14)$$

in which $C_i = \cos(i)$ and $S_i = \sin(i)$, calculated in different directions of the coordinate system, and t represents the level set parameter. Satisfying Eqs. 9–14 yields infinite surfaces indicating various TPMS structures. The inequalities ($f < t$) and ($f > t$) result in two solid phases,

referred to as Endo-Skeleton and Exo-Skeleton structures, respectively. For each TPMS, there exists a distinct range of level set parameters within which the relative density—the ratio of solid-phase volume to the unit cell volume—for each skeletal phase is specified. Outside this range, the TPMS loses its bi-continuity. Table 1 indicates the range of level set parameter values and the corresponding relative densities of the skeletal phases for the 6 TPMS investigated in this study.

After introducing TPMS structures and highlighting their implicit functions, it becomes necessary to provide schematics to gain a better insight into them. Fig. 2 depicts the unit cell of each TPMS microstructure utilized in this research, along with their separate skeletal phases. For each schematic, the volume fraction (VF) of the skeletal phases is set at 50%.

2.2.2. Random heterogeneous microstructures

To conduct a comprehensive investigation of two-phase microstructure DEAs, random microstructures (R-DEAs) were introduced for comparison with P-DEAs across various criteria. The first, called the Random Checkerboard Microstructure (RCM), serves as a basic representation of heterogeneous materials. In this model, phase dispersion is entirely random, based on the specified volume fractions of each phase. These microstructures are generated using a Python script that defines a 3D random array with specific dimensions, containing values of 0 and 1.

The second random microstructure used in the present work is the Anisotropic Heterogeneous Microstructure (AHM). A previously developed method was utilized to create three-dimensional (3D) microstructures exhibiting preferential anisotropic behavior. Eigen microstructures were effectively realized by integrating Monte Carlo and Cellular Automata algorithms. The reconstruction process is carried out in three iterative steps: cell generation, distribution, and growth. In this approach, the initial geometries are defined by primary cells, which are placed at random nucleation points determined by the volume fractions of each phase. The growth of these cells is simulated using Cellular Automata algorithms. Additionally, by adjusting the cell growth parameters in different directions, the anisotropy of each phase can be precisely controlled.

The detailed methodologies and algorithms for microstructure generation have been thoroughly discussed in our previous publication, providing a comprehensive framework for understanding and replicating this innovative approach (Baniassadi et al., 2011). For a clearer perspective on these microstructures, Fig. 3 showcases voxel-based R-DEAs generated by the Python script.

2.3. Finite element modeling

In this study, all finite element analyses were conducted using the commercial software ABAQUS. To facilitate efficient and straightforward parametric studies, a Python script was developed to define ge-

Table 1

The level set parameter range (t) and the associated volume fraction (VF) of the skeletal phases for the TPMS structures.

Structure	t [-]	VF [%]
Schwarz-P	[−1.0, 1.0]	[21.3, 78.7]
Gyroid	[−1.4, 1.4]	[2.2, 97.8]
Schwarz-D	[−0.99, 0.99]	[8.5, 91.5]
IWP	[−2.99, 2.99]	[0.8, 89.8]
FRD	[−1.1, 1.0]	[21.4, 66.7]
Neovius	[−0.75, 0.75]	[33.3, 66.2]
Octo	[−0.22, 0.05]	[47.5, 76.0], [22.75, 47.5] ^{a,b}
C (D)	[−0.16, 0.16]	[37.5, 62.5] ^b

^a The bi-continuity ranges of the Exo-skeletal and Endo-Skeletal phases in the Octo structure were denoted, respectively. For other structures, the range is the same for both Exo-skeletal and Endo-Skeletal phases.

^b These ranges were evaluated approximately.

Table 2

The material parameters of the silicone elastomers used as solid phases. Shear modulus and material permittivity values were obtained from reference (Hajiesmaili and Clarke, 2021).

Material	Shear Modulus (kPa)	Material Permittivity (pF/mm)
PDMS-Sylgard™ 10:1	440	2.7
Ecoflex™	100	3.2

* Poisson's ratios of the materials were set as 0.475 in simulations.

ometries and other relevant aspects of the analysis in ABAQUS. As the first step of the analysis, voxel-based TPMS geometries were defined. These geometries feature cubic unit cells with dimensions $L_x = 2\pi l_x$, $L_y = 2\pi l_y$, and $L_z = 2\pi l_z$, where $2\pi l_i$ denotes the length of the unit cell in different directions. Each unit cell is discretized into N_x , N_y , and N_z voxels in each direction. The coordinates of the center of each voxel, multiplied by $\alpha_i = L_i/N_i$, are in Eqs. 9–14 as (x, y, z) . As the number of voxels increases, the accuracy of the TPMS geometry improves.

Next, appropriate materials were assumed for both introduced phases. In this work, two commercial silicone elastomers were used as the Endo-Skeletal and Exo-Skeletal phases. Additionally, fully compliant electrodes were assumed for each structure to avoid constraining the actuation. Table 2 provides the material parameters for the silicone elastomers.

As the next step, the governing equations for the problem of DEAs under large deformations were defined for each element using a User-Defined Elements (UEL) subroutine written by Hajiesmaili and Clarke (2021). This UEL subroutine was verified by comparing the analytical solution of a single-phase rectangular DEA with the FEM solution. Both analyses utilized Ecoflex as the dielectric elastomer (see Table 2). However, while the analytical solution assumed incompressibility ($J = 1$) for the layer, the FEM solution treated the material as nearly incompressible (with a Poisson's ratio of 0.475). A good agreement was observed between the results, as shown in Fig. 4.

To provide further detail, it is important to note that the Coupled Temperature-Displacement scheme was selected to define the "Step" procedure due to its similarity to the coupled electromechanical problem in the governing equations. Consequently, the UEL subroutine exclusively evaluated electric field-induced stresses and their contribution to the governing equations. Utilizing a reduced integration scheme, each voxel was modeled as a trilinear brick element (C3D8RT) throughout the analyses. Table 3 outlines the algorithm implemented in the UEL subroutine to solve the problem at each increment.

To conduct reliable research and present robust results, mesh sensitivity analysis of all TPMS geometries was performed. The results revealed that a mesh with dimensions of $30 \times 30 \times 30$ elements (totaling 27,000 elements) is suitable for P-DEAs, while a mesh with dimensions of $50 \times 50 \times 50$ elements (totaling 125,000 elements) is appropriate for R-DEAs. Since the present work is comparative in nature, a single unit cell structure ($1 \times 1 \times 1$) was employed for all representative volume elements (RVEs), and tessellation sensitivity analysis was disregarded. To avoid dimension dependency of the results, the length of all RVEs was set at $100 \mu\text{m}$ in each direction. Additionally, from now on, Ecoflex material is assigned to the exo-skeletal phase, and its proportion serves as the reference for volume fraction evaluation in all RVEs.

3. Results and discussion

This section reports the results of actuation performance and blocking forces for all microstructures. Additionally, field localization in both P-DEAs and R-DEAs is investigated, offering valuable insights into the potential failure mechanisms of each candidate. Furthermore, the results are discussed to enhance our understanding of the effectiveness of microstructure DEAs. The investigations of this section are conducted through two case studies: equibiaxial actuation of microstructures without pre-stresses and uniaxial actuation of microstructures subjected

to pre-stresses. Fig. 5 illustrates the electromechanical constraints imposed on a typical representative microstructure in both case studies. In both cases, electrical loading is applied by imposing a constant electric field on the upper side of all investigated RVEs. This approach ensures consistency and prevents load dependency in the case studies. It is noteworthy that the results presented in the following subsections depend on material and geometric characteristics. Therefore, comparative discussion is critical for this study. As a result, valuable qualitative insights can be drawn.

3.1. Actuation performance

One of the most critical factors in DEAs is achieving high actuation performance at low voltages. To address this, novel DEA composites have been proposed. In the present work, a specific type of DEA composites, known as P-DEAs, is focused on. The homogenized actuation performance of P-DEAs is investigated by solving the equibiaxial actuation problem. The homogenization process is conducted by measuring average stretches in each direction during electromechanical loading. Additionally, voltage-related differences are assessed by comparing electric potentials between the top and bottom surfaces of each RVE at various increments.

The results indicate that incorporating materials with higher permittivity and lower stiffness into two-phase dielectric elastomer actuators (P-DEAs) leads to a significant reduction in operational voltages for the microstructure. Notably, this actuation enhancement is closely tied to the volume fraction of the constituent phases. Fig. 6a illustrates the actuation performance of IWP (a well-known TPMS) at various volume fractions, demonstrating its relationship with operational voltages. As evident, the actuation performance of IWP is strongly correlated with its base phases. This trend holds true for other P-DEAs as well, albeit with minor variations. Approximated electrical breakdown contours for silicones, obtained from reference (Vaicekauskaitė et al., 2020), which provide valuable insights into the practical usage of DEAs, are presented. Numerical instabilities are observed at volume fractions of 50% and 75%, which hindered further voltage-stretch tracking. Nevertheless, consistent trends across all volume fractions underscore the efficiency of P-DEAs.

In Fig. 6b, the operational voltages for IWP are illustrated at a given stretch ($\lambda_x = 1.1$) across different volume fractions. As evident, when 25% Ecoflex is added to the IWP microstructure (where Sylgard is the dominant phase), actuation performance is improved by up to 15.8%. At a volume fraction of 50%, this enhancement can be reached up to 31.1%. Further increasing Ecoflex to 75% boosts performance to 43.2%. Customization is possible by adjusting electromechanical characteristics and phase volume fractions.

To achieve a deeper understanding of P-DEAs' performance in comparison with other architected microstructures and to highlight their exceptional actuation capabilities, a comprehensive investigation was conducted. Specifically, two types of random microstructures (R-DEAs), namely RCM and AHM, were introduced. Subsequently, the actuation performance of all microstructures was analyzed by solving the equibiaxial actuation problem. Fig. 7 illustrates the homogenized operational voltages required for all microstructures to achieve a lateral stretch of $\lambda_x = 1.1$ across three different volume fractions.

Among all microstructures, Octo has the best average actuation performance across all volume fractions. At VF 25%, RCM requires 7.32 kV to reach a 1.1 lateral stretch, while Octo outperforms it by up to 6.2%. At VF 50%, the overall trend remains consistent with VF 25%. However, the percentage change for Octo, as the best microstructure relative to RCM (the worst microstructure), increases to 9.9%. At VF 75%, the trend shifts slightly, and FRD demonstrates better actuation performance. Nevertheless, the differences between FRD and Octo are minimal. In this volume fraction, FRD shows an 8.9% improvement relative to RCM, which possesses the poorest actuation performance.

As evident, R-DEAs exhibit inferior actuation performance compared

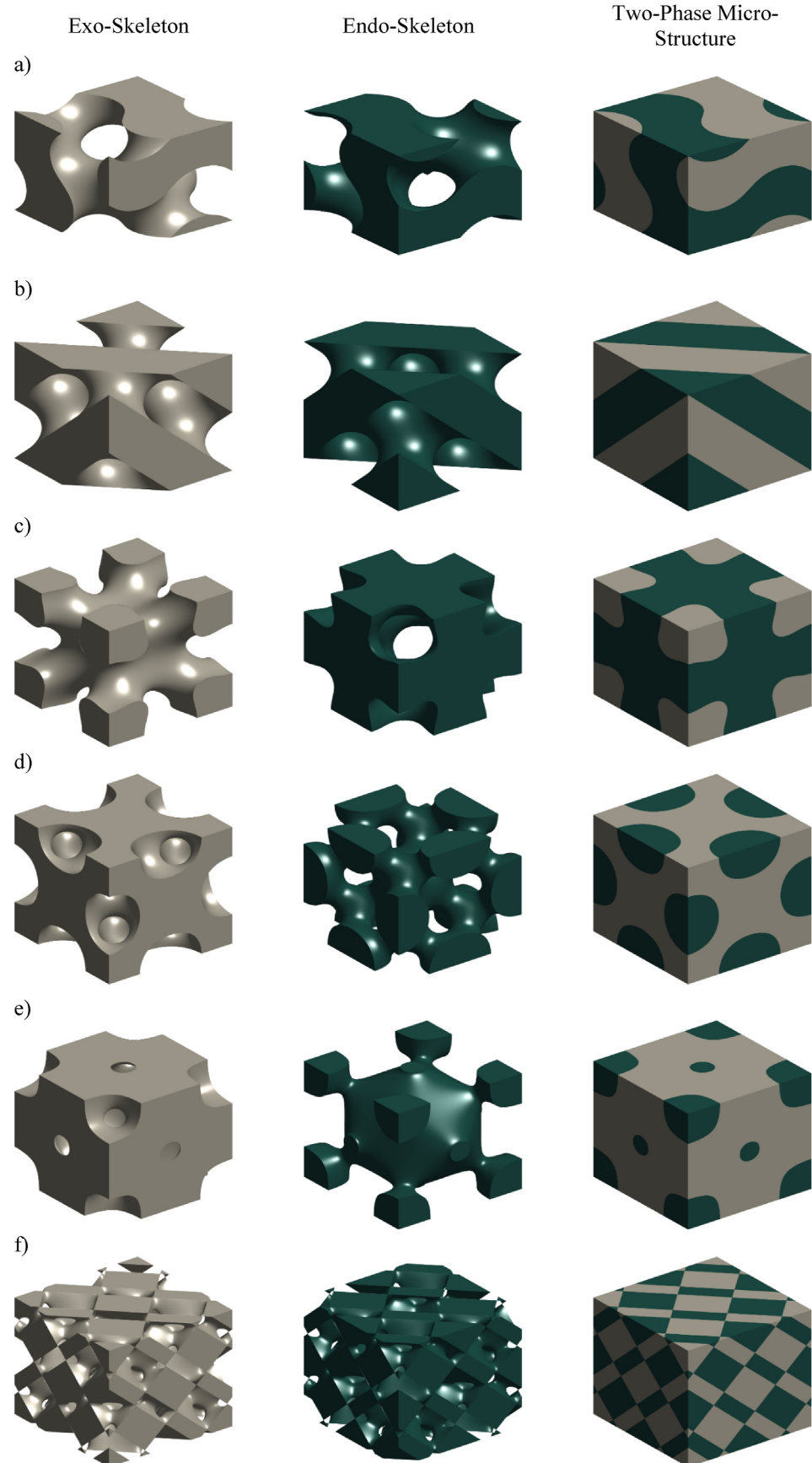


Fig. 2. The unit cell of P-DEA two-phase microstructures: a) Gyroid, b) Sch-D, IWP, d) FRD, e) Octo, and f) C(D). Each microstructure displays individual skeletal phases—Exo-Skeleton and Endo-Skeleton. Both phases contribute equally, with a 50% volume fraction.

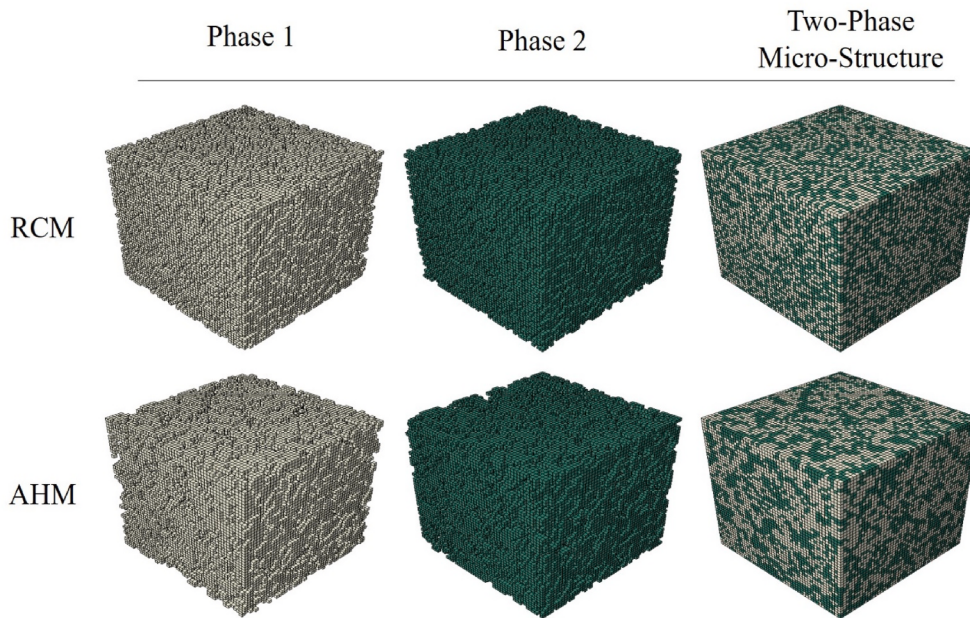


Fig. 3. Voxel-based R-DEAs investigated in this study, with dimensions of $50 \times 50 \times 50$. Both structures were generated using a Python script.

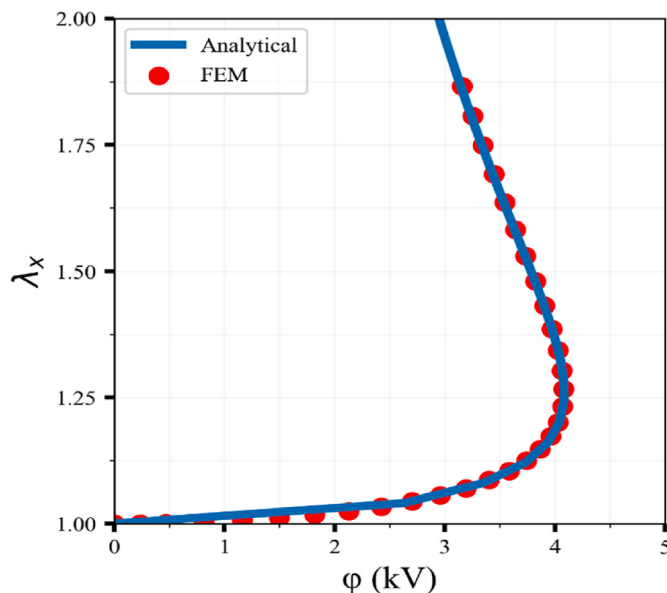


Fig. 4. Verification results of the UEL subroutine for a single-phase rectangular DEA. Ecoflex was used as the dielectric elastomer (see Table 2), with the distinction that the analytical solution assumed incompressibility for the DEA.

to P-DEAs across all investigated volume fractions, implying an inherent superiority of P-DEAs in terms of actuation. Interestingly, this advantage persists even when the microstructures lose their bi-continuity, a characteristic typically considered unfavorable for a microstructure. Examples of this behavior can be seen in C(D) and Octo at 25% and 75% volume fractions. The primary reason for this superiority is that TPMS geometries are more ordered compared to their random counterparts. Although this uniformity leads to higher moduli in problems involving purely mechanical loadings, the same trend is not observed in P-DEAs. This is mainly because the dominant regime of deformation in DEAs is electrical. Furthermore, as the through-thickness electric field flows more effectively within the microstructure, lateral stretches are higher. Consequently, P-DEAs, with more uniform phase dispersion in their microstructure, may benefit from improved through-thickness electric

Table 3

FEM analysis algorithm is utilized within the UEL subroutine for each increment.

FEM analysis Algorithm

1. Input: Material parameters, specified BCs.
2. Output: Stretches, voltages, electric fields.
1. Begin
2. Define the inputs and create a job through a python script, calling the UEL File.
3. Calculate the Electric Field (E) from nodal voltages.
4. Calculate $\sigma^{Maxwell}$ and add it to σ^{total} .
5. Complete the stiffness matrix and the residual vector with the additional terms from $\sigma^{Maxwell}$.
6. Solve the non-Linear algebraic system of equations using the Newton-Raphson method.
7. Write the Outputs for the pseudo-elements.
8. End

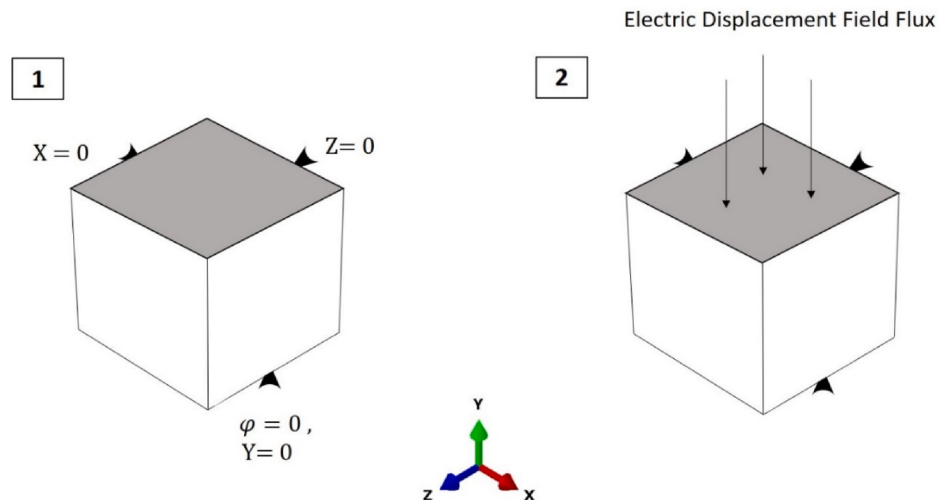
field flow, resulting in higher actuation.

3.2. Blocking force performance

Blocking force is considered one of the important characteristics of DEAs. Specifically, it refers to the maximum force that can be exerted by the actuator when its displacement is constrained to zero. DEAs with high blocking forces find practical applications in soft grippers (Shintake et al., 2016). In the previous section, the natural superiority of P-DEAs over R-DEAs was demonstrated. Therefore, in a comparative study, it is expected that for the same amount of initial total energy applied to the microstructures (the sum of mechanical and electrical energy), R-DEAs with lower actuation will exhibit higher blocking forces. In this section, the blocking forces of all two-phase microstructures—both periodic (P-DEAs) and random (R-DEAs)—as well as pure Ecoflex and Sylgard microstructures, were analyzed and compared by solving the uniaxial actuation of pre-stressed DEAs.

The reason a pre-stress is applied to the microstructures is that DEAs under pre-stress can significantly suppress electromechanical instability. This is due to the incorporation of strain-stiffening effects within the material. For this purpose, the microstructures under study were subjected to a pre-stress of 92.5 kPa in the lateral X-direction, though their actuation in this direction remained unrestricted during electromechanical loading (as shown in Fig. 5b). The process of measuring the

a)



b)

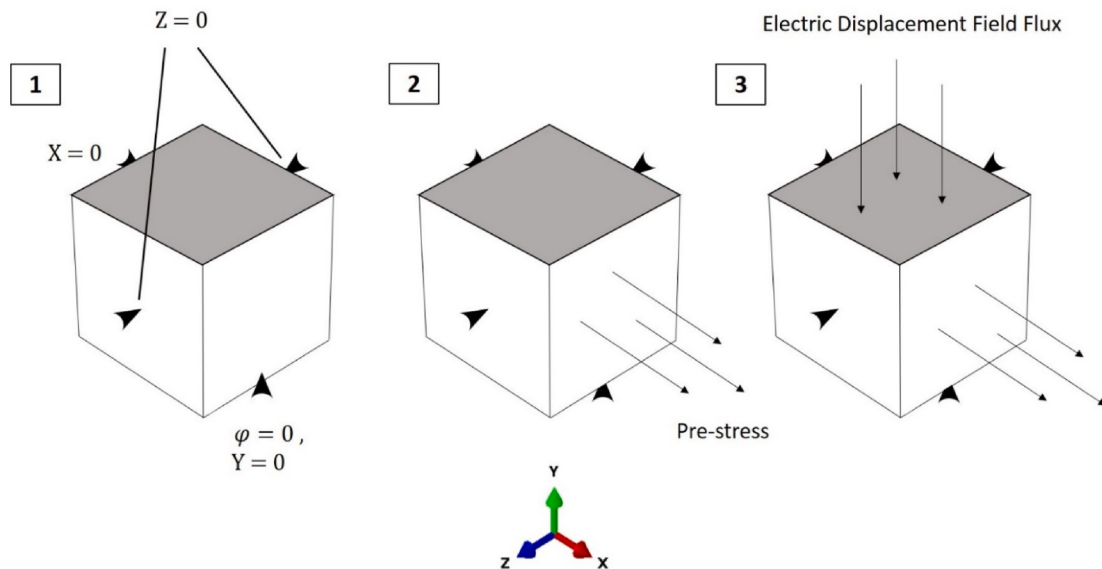


Fig. 5. The representation of a typical microstructure in each case study. (a) Equibiaxial actuation problem, where electromechanical BCs and electrical loading are shown in two steps, respectively. (b) Uniaxial actuation of pre-stressed RVEs, with BCs, pre-stresses, and electrical loading depicted in three steps, respectively.

blocking force proceeded as follows: the average stress exerted by the RVE in the X-direction was calculated and then multiplied by the instantaneous area of the X-plane of the RVE. Notably, the force corresponding to the pre-stress was subtracted from the homogenized blocking forces related to electrical loading.

First, the importance of two-phase microstructures in exerting forces must be highlighted. Fig. 8 illustrates the blocking forces exerted by pre-stressed base phases (Ecoflex and Sylgard) compared to pre-stressed IWP microstructures under 10% lateral actuation ($\lambda_x = 1.1$). It is important to note that pre-stressing induces varying pre-stretch values in the microstructures shown in the figure, and lateral actuation refers to actuation caused by electrical loading.

As shown in Fig. 8, introducing a stiffer phase with lower permittivity (Sylgard) into the DEA microstructures significantly affects their blocking force performance. For instance, incorporating 25% Sylgard into IWP microstructures nearly doubles the blocking force compared to pure Ecoflex. Moreover, microstructures with 75% Sylgard exhibit blocking forces that are around five times higher than those of pure Ecoflex.

After demonstrating the significant potential of two-phase

microstructure DEAs in terms of blocking forces, it is now important to compare random-based and architected microstructures in this context. Fig. 9 presents the blocking forces exerted by all two-phase microstructures at a lateral stretch of 1.1, considering volume fractions of 25%, 50%, and 75%.

As expected, R-DEAs exhibit a higher blocking force response compared to P-DEAs across all volume fractions (see Fig. 9). When comparing the best-performing P-DEAs at different volume fractions with RCM (the top microstructure in terms of blocking force), it is found that at a 50% volume fraction, RCM outperforms IWP (the best P-DEA) by 10.9%. This performance gap narrows to 6.2% at a 25% volume fraction and 6.9% at a 75% volume fraction. On average, IWP performs better among P-DEAs, though at a 25% volume fraction, C(D) shows higher forces.

While the blocking forces of R-DEAs are superior to that of P-DEAs, TPMS-based microstructures have the advantage of being mathematically definable, making optimization of their blocking force performance more accessible (Ma et al., 2023). This intrinsic advantage of P-DEAs over their counterparts warrants further investigation.

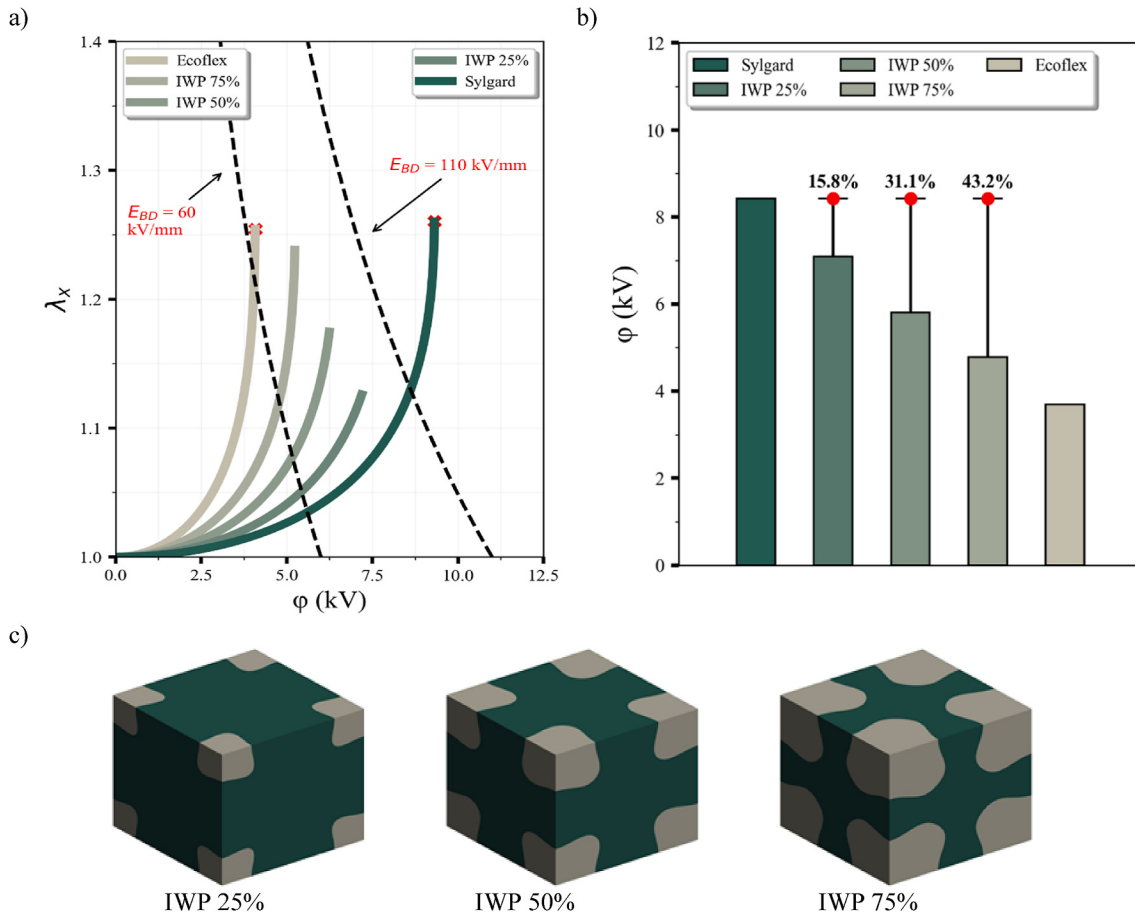


Fig. 6. a) Voltage versus lateral stretch plot for IWP across different volume fractions. The figure shows approximated electrical breakdown contours (Vaicekauskaitė et al., 2020). b) Bar plot illustrating operational voltages for IWP at a given stretch ($\lambda_x = 1.1$) across different volume fractions. Percentage changes for each microstructure are shown relative to Sylgard c) Schematics of the two-phase IWP microstructures at volume fractions of 25%, 50%, and 75%.

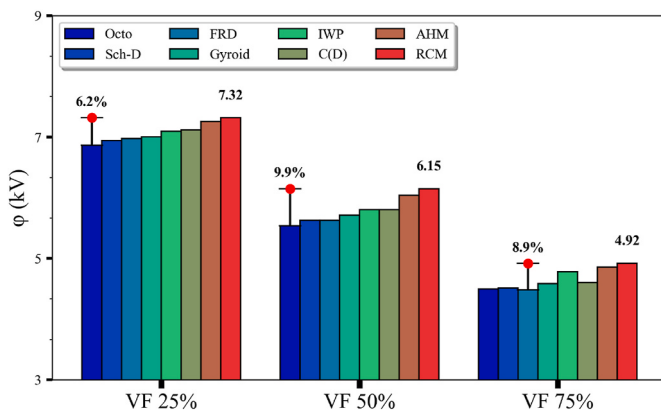


Fig. 7. Bar plot showing the operational voltages for all investigated microstructures at a lateral stretch of $\lambda_x = 1.1$ for volume fractions of 25%, 50%, and 75%. The operational voltage value of RCM is displayed alongside the percentage change of Octo relative to RCM in each volume fraction.

3.3. Localized electric fields

One of the disadvantages associated with two-phase DEAs is the occurrence of localized electric fields resulting from material variations within the structures. While homogenized electric fields contribute to the overall actuation performance of microstructures, the presence of such fields can also lead to electrical breakdown of the material.

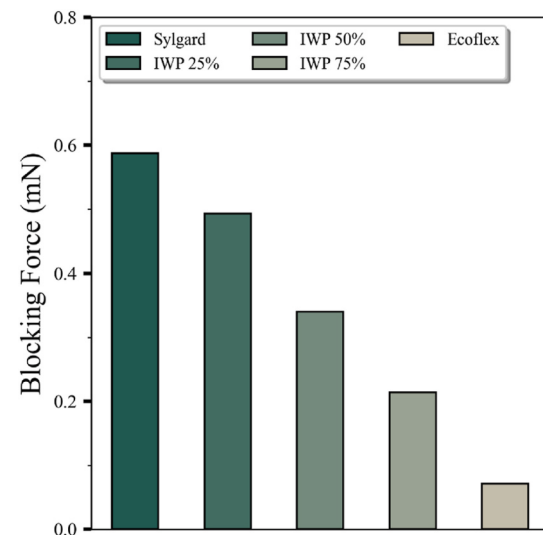


Fig. 8. Comparison of the blocking forces of pre-stressed base phases (Ecoflex and Sylgard) with pre-stressed IWP microstructures under 10% lateral actuation ($\lambda_x = 1.1$).

Therefore, reducing these fields may enhance the electromechanical performance of DEAs, making them more practical. The magnitude of these fields can be measured using various localization indexes. In this study, the Electric Displacement Field Localization Index (D_{Index}) is

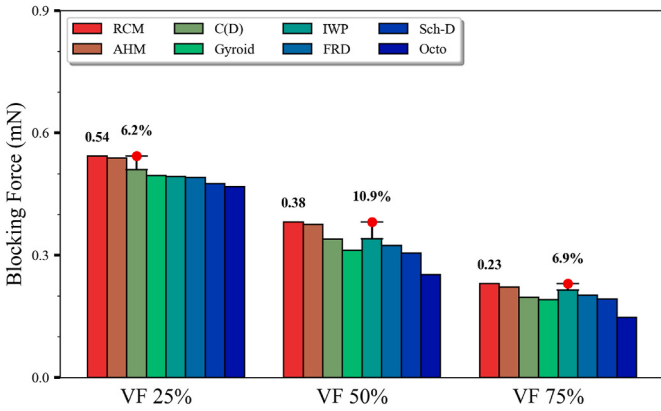


Fig. 9. Bar plot of blocking forces exerted by all microstructures at a lateral stretch of $\lambda_x = 1.1$ for volume fractions of 25%, 50%, and 75%. The figure also shows the blocking force value of RCM alongside the percent change of the P-DEA with the highest blocking force in each volume fraction.

utilized. As mentioned in the previous section, the electric displacement field can be defined as $\vec{D} = \epsilon \vec{E}$, and the D_{index} is given by $D_{\text{index}} = D_{\max}/D_{\text{avg}}$. Here, D_{\max} represents the magnitude of the maximum electric displacement field vector occurring within the structure, while D_{avg} corresponds to the magnitude of the average electric displacement field across the entire microstructure. Notably, when the D_{index} approaches unity, it indicates lower gradients of electric fields, resulting in reduced failure probabilities. To explore these gradients, the D_{index} for all the aforementioned microstructures was analyzed by solving the problem of equibiaxial actuation in microstructures (see Fig. 5a). During this process, the variables D_{\max} and D_{avg} were extracted at each increment using an appropriate Abaqus script. Fig. 10 illustrates the D_{index} for each microstructure concerning lateral actuation across three volume fractions.

The D_{index} trends vary based on the volume fraction and stretch, indicating complex behavior in two-phase microstructures in response to electromechanical loading. However, it is evident that D_{index} values increase as the amount of stretch increases. As illustrated in Fig. 10, at VF 25%, the best performance (lowest failure possibility) is attributed to

IWP, while the worst performance (highest failure possibility) is associated with C(D). At VF 50%, trends exhibit slight variation, with FRD and Octo showing the best and worst performance, respectively. Finally, at VF 75%, the highest and lowest D_{index} values are observed for C(D) and RCM, respectively. At VF 50%, premature numerical instability occurs before electromechanical instability in Octo and Gyroid, limiting further analysis. This phenomenon persists for Gyroid, Octo, Sch-D, and AHM at VF 75%, highlighting the complexity of the problem in terms of numerical analysis.

One contributing factor to the high D_{index} values may be the presence of abrupt phase changes within the microstructures. For instance, C(D) across all volume fractions, as well as Octo at 25% and 50% volume fractions, exhibit poor field localization performance, primarily due to numerous phase changes within their microstructures. However, for Octo at 75% volume fraction, the trend shifts, and Octo demonstrates lower D_{index} values. This shift is attributed to the microstructure losing its bi-continuity, thereby eliminating the abrupt phase changes. To better understand these observations, it is useful to examine the electric displacement field contours within the aforementioned microstructures.

Fig. 11 presents the electric displacement field contours in the RVEs of C(D) and Octo at a 50% volume fraction.

As evident in Fig. 11, high electric displacement fields are observed at abrupt phase changes from Sylgard, which has lower permittivity, to Ecoflex, which has higher permittivity. These abrupt changes lead to local electric field concentrations, resulting in high D_{index} values. In contrast to P-DEAs, a microstructure with completely random phase dispersion (RCM) exhibits good field localization performance (see Fig. 10). Although constant phase changes occur within its microstructure, none of the phases form agglomerations, and consequently, electric field concentration is negligible. This behavior results in low D_{index} values. However, AHM, as an anisotropic case of random microstructures, shows moderate D_{index} values. Therefore, the significant superiority of R-DEAs over P-DEAs cannot be concluded, and the results are comparable.

4. Conclusion

This study investigated the homogenized performance of two-phase microstructure DEAs with TPMS geometries, referred to as P-DEAs. By

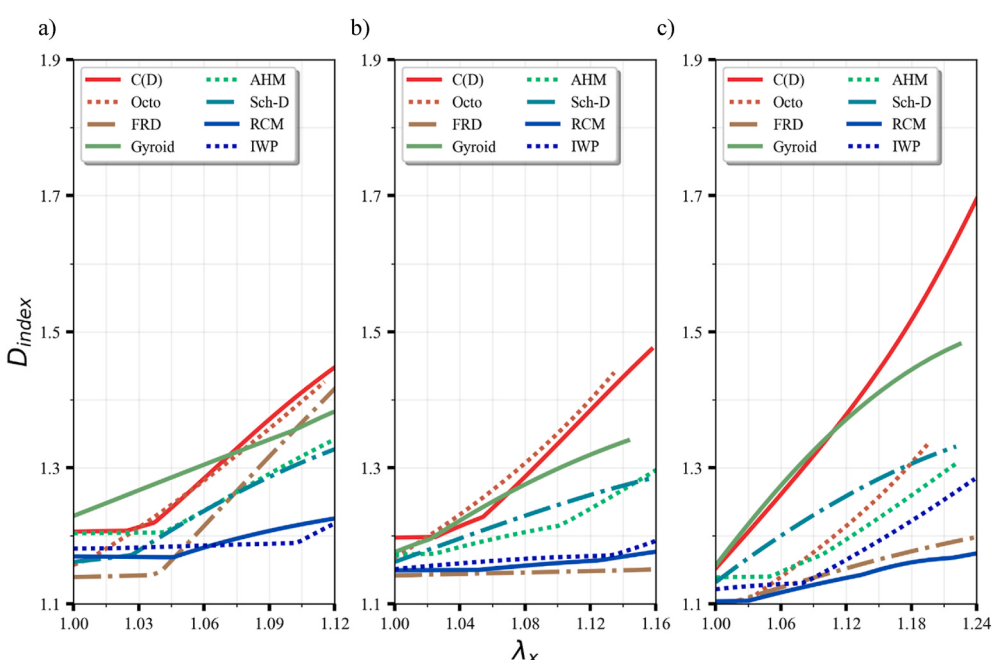


Fig. 10. D_{index} versus lateral stretches (λ_x) for all investigated microstructures at volume fractions of a) 25%, b) 50%, and c) 75%.

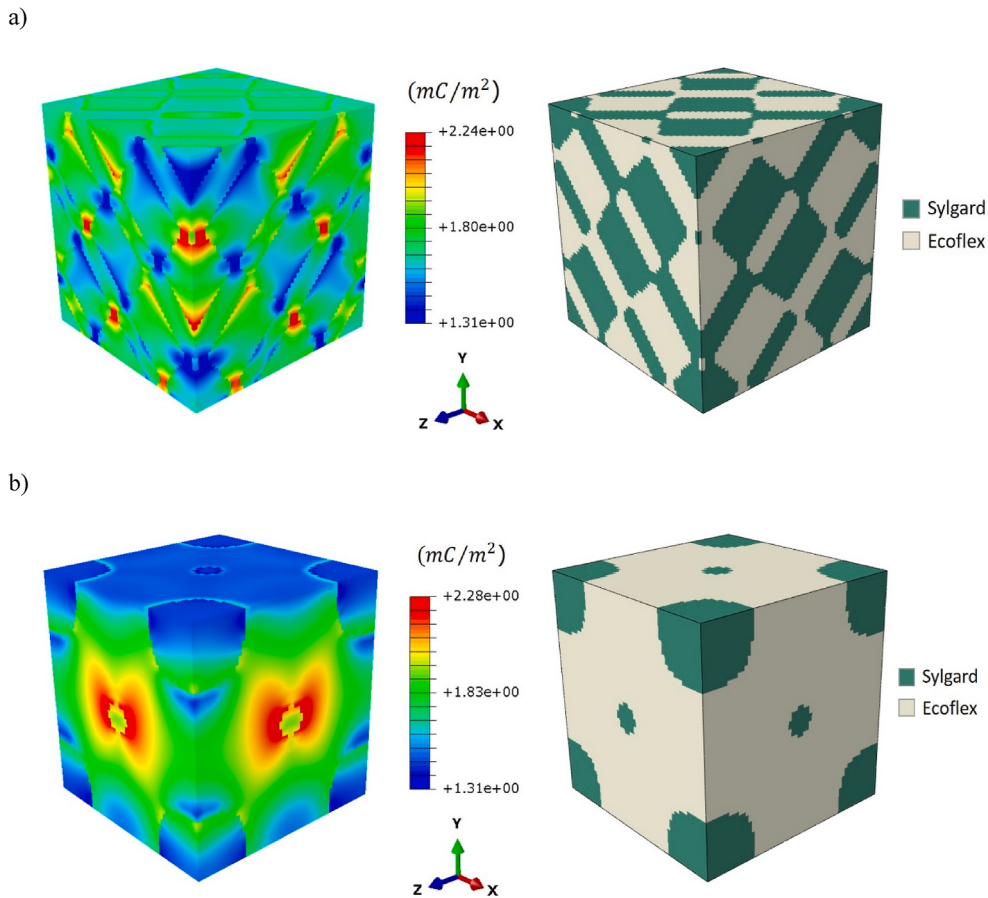


Fig. 11. Electric displacement field contours for the microstructures with the highest D_{index} values at 50% volume fraction. Including: a) C(D), b) Octo. For each microstructure, $\lambda_x = 1.1$ is set.

incorporating phases with higher permittivity and lower stiffness into the microstructures, significant improvements in actuation at lower voltages were observed. For example, when 25% Ecoflex was incorporated into the IWP microstructure (whose dominant phase was Sylgard), the actuation performance improved by up to 15.8%. Furthermore, this enhancement increased to 43.2% by adding 75% Ecoflex to the microstructure. In conclusion, the actuation performance of microstructure DEAs can be customized based on the volume fraction of phases and the introduction of various materials into the microstructures. To conduct a more comprehensive investigation, two types of random microstructures (R-DEAs) were introduced and compared with P-DEAs in terms of actuation, blocking force, and field localization across three different volume fractions.

Among the microstructures, P-DEAs consistently outperformed R-DEAs in actuation performance. Octo demonstrated the best performance, showing a maximum improvement of 9.9% compared to RCM, the worst-performing microstructure, at a volume fraction of 50%. The intrinsic superiority of P-DEAs was attributed to the uniformity of phase dispersion and the ordered flow of the electric field within them. However, in terms of blocking force, R-DEAs outperformed the selected P-DEAs. Notably, the IWP microstructure among P-DEAs exhibited the highest average blocking force.

For the last criterion, it was found that both RCM and IWP microstructures had the lowest electric displacement field differences within them, while C(D) exhibited the highest differences, leading to large D_{index} values. It was concluded that harsh phase changes within a microstructure contributed to high D_{index} values. Fig. 12 provides a qualitative comparison of DEA performance in terms of actuation, blocking force, and field localization.

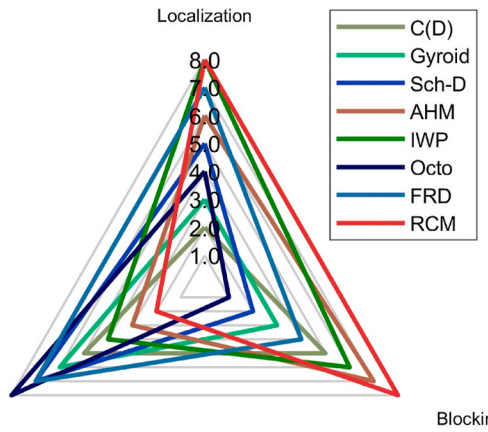


Fig. 12. Spider plot comparing microstructures based on actuation, field localization, and block force criteria, qualitatively. Performance is rated on a scale from 1 (lowest) to 8 (highest) using a non-one-to-one scheme.

microstructures was evaluated on a scale from 1 to 8, where 1 corresponds to the lowest performance and 8 to the highest.

5. Limitations and outlook

This study takes an initial step toward a novel concept for enhancing the behavior of multi-phase DEA composites with intricate architectures. The results contribute to a deeper understanding of the electro-mechanical behavior of multi-phase microstructure DEAs, forming a

basis for further exploration. Future research can focus on optimizing these microstructures using genetic algorithms to enhance performance. Surrogate models, as a novel topic, is also recommended to be developed so that the multi-physics behavior of DEAs with architected geometries can be predictable.

However, several numerical and experimental challenges remain to be addressed. For instance, more accurate models incorporating precise geometries and periodic boundary conditions, which were not considered in this study, are essential for advancing the field. More advanced assumptions can be considered in terms of elastomeric materials polarization, as well. Additionally, experimental validation is necessary to confirm the significant potential of embedding TPMS architectures in DEAs. This task is inherently challenging, primarily due to the difficulties in 3D printing soft, elastomeric, multi-material structures with complex geometries like TPMS. However, recent advancements in this area show promise (Karamzadeh et al., 2024), (Wang et al., 2024).

CRediT authorship contribution statement

Mohammad Ali Safaei: Writing – original draft, Validation, Software, Methodology, Investigation, Formal analysis, Conceptualization. **Mostafa Baghani:** Writing – review & editing, Supervision, Methodology, Investigation, Formal analysis. **Majid Baniassadi:** Writing – review & editing, Supervision, Methodology, Investigation, Formal analysis. **Mahdi Bodaghi:** Writing – review & editing, Supervision, Methodology, Investigation, Formal analysis.

Declaration of competing interest

The authors declare that they have no known competing financial interests or personal relationships that could have appeared to influence the work reported in this paper.

Data availability statement

All relevant codes are available in the following GitHub repository: <https://github.com/mohsafaei/DEAs.git>.

References

- Ahangari, A., Doostmohammadi, H., Baniassadi, M., Bodaghi, M., Baghani, M., 2024. Development and 4D printing of magneto-responsive PMMA/TPU/Fe3O4 nanocomposites with superior shape memory and toughness properties. *Eur. Polym. J.* 220, 113495. <https://doi.org/10.1016/j.eurpolymj.2024.113495>.
- Ahmadi, A., Asgari, M., 2020. Nonlinear coupled electro-mechanical behavior of a novel anisotropic fiber-reinforced dielectric elastomer. *Int J Non Linear Mech* 119. <https://doi.org/10.1016/j.ijnonlinmec.2019.103364>.
- An, L., Wang, F., Cheng, S., Lu, T., Wang, T.J., 2015. Experimental investigation of the electromechanical phase transition in a dielectric elastomer tube. *Smart Mater. Struct.* 24 (3), 035006. <https://doi.org/10.1088/0964-1726/24/3/035006>.
- Askari-Sedeh, M., Baghani, M., 2023. pH-Sensitive Hydrogel Bilayers: investigation on Transient Swelling-induced Bending through analytical and FEM approaches. *Gels* 9 (7). <https://doi.org/10.3390/gels9070563>.
- Bahreman, M., Arora, N., Darijani, H., Rudykh, S., 2022. Structural and material electro-mechanical instabilities in microstructured dielectric elastomer plates. *Eur. J. Mech. Solid.* 94, 104534. <https://doi.org/10.1016/j.euromechsol.2022.104534>.
- Baniassadi, M., Garmestani, H., Li, D.S., Ahzi, S., Khaleel, M., Sun, X., 2011. Three-phase solid oxide fuel cell anode microstructure realization using two-point correlation functions. *Acta Mater.* 59 (1), 30–43. <https://doi.org/10.1016/j.actamat.2010.08.012>.
- Behera, S.K., Kumar, D., Sarangi, S., 2021. Modeling of electro-viscoelastic dielectric elastomer: a continuum mechanics approach. *Eur. J. Mech. Solid.* 90, 104369. <https://doi.org/10.1016/j.euromechsol.2021.104369>.
- Chen, F., Miao, Y., Zhang, L., Chen, S., Zhu, X., 2022. Triply periodic Channels enable soft Pneumatic linear actuator with single material and Scalability. *IEEE Robot Autom Lett* 7 (2), 2668–2675. <https://doi.org/10.1109/LRA.2022.3143292>.
- Corkery, R.W., Tyrode, E.C., 2017. On the colour of wing scales in butterflies: iridescence and preferred orientation of single gyroid photonic crystals. *Interface Focus* 7 (4), 20160154. <https://doi.org/10.1098/rsfs.2016.0154>.
- Duduta, M., Hajiesmaili, E., Zhao, H., Wood, R.J., Clarke, D.R., 2019. Realizing the potential of dielectric elastomer artificial muscles. *Proc. Natl. Acad. Sci. USA* 116 (7), 2476–2481. <https://doi.org/10.1073/pnas.1815053116>.
- Enferadi, A., Baniassadi, M., Baghani, M., 2024. Innovative multiphysics approach for designing high-performance thermo-responsive shape memory polymer microvalve. *Eur. J. Mech. Solid.* 103, 105174. <https://doi.org/10.1016/j.euromechsol.2023.105174>.
- Feng, J., Fu, J., Yao, X., He, Y., 2022. Triply periodic minimal surface (TPMS) porous structures: from multi-scale design, precise additive manufacturing to multidisciplinary applications. *Int. J. Extrem. Manuf.* 4 (2), 022001. <https://doi.org/10.1088/2631-7990/ac5be6>.
- Feng, W., et al., 2024. A large-strain and ultrahigh energy density dielectric elastomer for fast moving soft robot. *Nat. Commun.* 15 (1), 4222. <https://doi.org/10.1038/s41467-024-48243-y>.
- Firoozan, M., Baniassadi, M., Baghani, M., Chortos, A., 2024. In silico optimization of aligned fiber electrodes for dielectric elastomer actuators. *Sci. Rep.* 14 (1), 4703. <https://doi.org/10.1038/s41598-024-54931-y>.
- Fisher, J.W., Miller, S.W., Bartolai, J., Simpson, T.W., Yukish, M.A., 2023. Catalog of triply periodic minimal surfaces, equation-based lattice structures, and their homogenized property data. *Data Brief* 49, 109311. <https://doi.org/10.1016/j.dib.2023.109311>.
- Gan, Z., Turner, M.D., Gu, M., 2016. Biomimetic gyroid nanostructures exceeding their natural origins. *Sci. Adv.* 2 (5), e1600084. <https://doi.org/10.1126/sciadv.1600084>.
- Gu, G.-Y., Gupta, U., Zhu, J., Zhu, L.-M., Zhu, X., 2017. Modeling of viscoelastic electromechanical behavior in a soft dielectric elastomer actuator. *IEEE Transactions on Robotics* 33 (5), 1263–1271. <https://doi.org/10.1109/TRO.2017.2706285>.
- Hajiesmaili, E., Clarke, D.R., 2019. Reconfigurable shape-morphing dielectric elastomers using spatially varying electric fields. *Nat. Commun.* 10 (1), 183. <https://doi.org/10.1038/s41467-018-08094-w>.
- Hajiesmaili, E., Clarke, D.R., 2021. Dielectric elastomer actuators. *J. Appl. Phys.* 129 (15), 151102. <https://doi.org/10.1063/5.0043959>.
- Hajiesmaili, E., Khare, E., Chortos, A., Lewis, J., Clarke, D.R., 2019. Voltage-controlled morphing of dielectric elastomer circular sheets into conical surfaces. *Extreme Mech Lett* 30, 100504. <https://doi.org/10.1016/j.eml.2019.100504>.
- Hajiesmaili, E., Larson, N.M., Lewis, J.A., Clarke, D.R., 2024. Programmed shape-morphing into complex target shapes using architected dielectric elastomer actuators. *Sci. Adv.* 8 (28), eabn9198. <https://doi.org/10.1126/sciadv.abn9198>.
- Han, L., Che, S., 2018. An overview of materials with triply periodic minimal surfaces and related geometry: from Biological structures to self-Assembled systems. *Adv. Mater.* 30 (17), 1705708. <https://doi.org/10.1002/adma.201705708>.
- Hu, W., Zhang, S.N., Niu, X., Liu, C., Pei, Q., 2014. An aluminum nanoparticle-acrylate copolymer nanocomposite as a dielectric elastomer with a high dielectric constant. *J Mater Chem C Mater* 2 (9), 1658–1666. <https://doi.org/10.1039/C3TC31929F>.
- Imanian, M.E., Kardan-Halvaei, M., Nasrollahi, F., Imanian, A., Montazerian, H., Nasrollahi, V., 2023. 3D printed flexible wearable sensors based on triply periodic minimal surface structures for biomonitoring applications. *Smart Mater. Struct.* 32 (1), 015015. <https://doi.org/10.1088/1361-665X/acab6c>.
- Ji, X., et al., 2021. Untethered Feel-through Haptics using 18-μm Thick dielectric elastomer actuators. *Adv. Funct. Mater.* 31 (39), 2006639. <https://doi.org/10.1002/adfm.202006639>.
- Kapfer, S.C., Hyde, S.T., Mecke, K., Arns, C.H., Schröder-Turk, G.E., 2011. Minimal surface scaffold designs for tissue engineering. *Biomaterials* 32 (29), 6875–6882. <https://doi.org/10.1016/j.biomaterials.2011.06.012>.
- Karamzadeh, V., et al., 2024. High-resolution additive manufacturing of a Biodegradable elastomer with A low-cost LCD 3D printer. *Adv Healthc Mater* 13 (9), 2303708. <https://doi.org/10.1002/adhm.202303708>.
- Khaleghi, S., Dehnavi, F.N., Baghani, M., Saifdari, M., Wang, K., Baniassadi, M., 2021. On the directional elastic modulus of the TPMS structures and a novel hybridization method to control anisotropy. *Mater. Des.* 210, 110074. <https://doi.org/10.1016/j.matdes.2021.110074>.
- Khaleghi, S., Baghani, M., Karimpour, M., Panahi, M.S., Wang, K., Baniassadi, M., 2023. Novel modified triply periodic minimal surfaces (MTPMS) developed using genetic algorithm. *J. Mater. Res. Technol.* 26, 2881–2906. <https://doi.org/10.1016/j.jmrt.2023.08.040>.
- Li, Q., et al., 2017. Bottlebrush elastomers: a new platform for freestanding electroactuation. *Adv. Mater.* 29 (2).
- Li, W., Yu, G., Yu, Z., 2020. Bioinspired heat exchangers based on triply periodic minimal surfaces for supercritical CO₂ cycles. *Appl. Therm. Eng.* 179, 115686. <https://doi.org/10.1016/j.applthermaleng.2020.115686>.
- Liu, K., Chen, S., Chen, F., Zhu, X., 2020. A Unidirectional soft dielectric elastomer actuator enabled by Built-in Honeycomb Metastructures. *Polymers* 12 (3). <https://doi.org/10.3390/polym12030619>.
- Liu, L., Han, Y., Xing, Z., Yong, H., 2022. Nonlinear deformation and instability of a dielectric elastomer tube actuator. *Int J Non Linear Mech* 147, 104235. <https://doi.org/10.1016/j.ijnonlinmec.2022.104235>.
- Long, X., Chong, K., Su, Y., Du, L., Zhang, G., 2023. Connecting the macroscopic and mesoscopic properties of sintered silver nanoparticles by crystal plasticity finite element method. *Eng. Fract. Mech.* 281, 109137. <https://doi.org/10.1016/j.engfractmech.2023.109137>.
- Lu, C., Zhang, C., Wen, P., Chen, F., 2021. Mechanical behavior of Al-Si10-Mg gyroid surface with variable topological parameters fabricated via laser powder bed fusion. *J. Mater. Res. Technol.* 15, 5650–5661. <https://doi.org/10.1016/j.jmrt.2021.11.008>.
- Ma, X., Guo, C., Hu, C., Zhang, Z., Shen, J., 2023. Study on the topological morphology and mechanical properties of variable-amplitude TPMS structures. *J. Mater. Res. Technol.* 27, 3459–3472. <https://doi.org/10.1016/j.jmrt.2023.10.164>.
- Madsen, F.B., Daugaard, A.E., Hvilsted, S., Skov, A.L., 2016. The current state of silicone-based dielectric elastomer transducers. *Macromol. Rapid Commun.* 37 (5), 378–413. <https://doi.org/10.1002/marc.201500576>.

- Maskery, I., et al., 2017. Insights into the mechanical properties of several triply periodic minimal surface lattice structures made by polymer additive manufacturing. *Polymer (Guildf)* 152. <https://doi.org/10.1016/j.polymer.2017.11.049>.
- Moretti, G., Rosset, S., Vertechy, R., Anderson, I., Fontana, M., 2020. A review of dielectric elastomer generator systems. *Advanced Intelligent Systems* 2 (10), 2000125. <https://doi.org/10.1002/aisy.202000125>.
- Niu, X., Stoyanov, H., Hu, W., Leo, R., Brochu, P., Pei, Q., 2013. Synthesizing a new dielectric elastomer exhibiting large actuation strain and suppressed electromechanical instability without prestretching. *J. Polym. Sci. B Polym. Phys.* 51 (3), 197–206. <https://doi.org/10.1002/polb.23197>.
- Pelrine, R., Kornbluh, R., Pei, Q., Joseph, J., 2000. High-speed electrically actuated elastomers with strain greater than 100. *Science* 287 (5454), 836–839, 1979.
- Pelrine, R., et al., 2002. Dielectric elastomer artificial muscle actuators: toward biomimetic motion. *Proc. SPIE* 4695, 126–137. <https://doi.org/10.1117/12.475157>.
- Racles, C., Cazacu, M., Fischer, B., Opris, D.M., 2013. Synthesis and characterization of silicones containing cyanopropyl groups and their use in dielectric elastomer actuators. *Smart Mater. Struct.* 22 (10), 104004. <https://doi.org/10.1088/0964-1726/22/10/104004>.
- Romasanta, L.J., Lopez-Manchado, M.A., Verdejo, R., 2015. Increasing the performance of dielectric elastomer actuators: a review from the materials perspective. *Prog. Polym. Sci.* 51, 188–211. <https://doi.org/10.1016/j.progpolymsci.2015.08.002>.
- Roudbarian, N., Jebellat, E., Famouri, S., Baniassadi, M., Hedayati, R., Baghani, M., 2022. Shape-memory polymer metamaterials based on triply periodic minimal surfaces. *Eur. J. Mech. Solid.* 96, 104676. <https://doi.org/10.1016/j.euromechsol.2022.104676>.
- Sadeghi, F., Baniassadi, M., Shahidi, A., Baghani, M., 2023. TPMS metamaterial structures based on shape memory polymers: mechanical, thermal and thermomechanical assessment. *J. Mater. Res. Technol.* 23, 3726–3743. <https://doi.org/10.1016/j.jmrt.2023.02.014>.
- Safavi, H.R., Amiri, A., Baniassadi, M., Zolfagharian, A., Baghani, M., 2023. An anisotropic constitutive model for fiber reinforced salt-sensitive hydrogels. *Mech. Adv. Mater. Struct.* 30 (23), 4814–4827. <https://doi.org/10.1080/15376494.2022.2106523>.
- Sang, L., et al., 2023. Reusability and energy absorption behavior of 4D-printed heterogeneous lattice structures based on biomass shape memory polyester. *J. Mater. Res. Technol.* 27, 1563–1578. <https://doi.org/10.1016/j.jmrt.2023.09.323>.
- Schoen, A.H., 1970. Infinite periodic minimal surfaces without self-intersections. <https://api.semanticscholar.org/CorpusID:119912824>.
- Shen, Z., Dong, R., Li, J., Su, Y., Long, X., 2024. Determination of gradient residual stress for elastoplastic materials by nanoindentation. *J. Manuf. Process.* 109, 359–366. <https://doi.org/10.1016/j.jmapro.2023.10.030>.
- Shintake, J., Rosset, S., Schubert, B., Floreano, D., Shea, H., 2016. Versatile soft grippers with intrinsic Electroadhesion based on multifunctional polymer actuators. *Adv. Mater.* 28 (2), 231–238. <https://doi.org/10.1002/adma.201504264>.
- Shirzad, M., Zolfagharian, A., Bodaghi, M., Nam, S.Y., 2023. Auxetic metamaterials for bone-implanted medical devices: recent advances and new perspectives. *Eur. J. Mech. Solid.* 98, 104905. <https://doi.org/10.1016/j.euromechsol.2022.104905>.
- Singh, D., Sharma, S., Kumar, R., Vaish, R., 2022. Representative volume element model of triply periodic minimal surfaces (TPMS)-based electrostrictive composites for numerical evaluation of effective properties. *Acta Mech.* 234, 1–21. <https://doi.org/10.1007/s00707-022-03404-2>.
- Suo, Z., 2010. Theory of dielectric elastomers. *Acta Mech. Solida Sin.* 23 (6), 549–578. [https://doi.org/10.1016/S0894-9166\(11\)60004-9](https://doi.org/10.1016/S0894-9166(11)60004-9).
- Tian, M., Yan, B., Yao, Y., Zhang, L., Nishi, T., Ning, N., 2014. Largely improved actuation strain at low electric field of dielectric elastomer by combining disrupting hydrogen bonds with ionic conductivity. *J Mater Chem C Mater* 2 (39), 8388–8397. <https://doi.org/10.1039/C4TC01140F>.
- Tian, R., et al., 2023. Dynamic crushing behavior and energy absorption of hybrid auxetic metamaterial inspired by Islamic motif art. *Appl. Math. Mech.* 44 (3), 345–362. <https://doi.org/10.1007/s10483-023-2962-9>.
- Vaickeauskaite, J., Mazurek, P., Vudayagiri, S., Skov, A.L., 2020. Mapping the mechanical and electrical properties of commercial silicone elastomer formulations for stretchable transducers. *J Mater Chem C Mater* 8 (4), 1273–1279. <https://doi.org/10.1039/C9TC05072H>.
- Wang, X., Liu, J., Dong, R., Gilchrist, M.D., Zhang, N., 2024. High-precision digital light processing (DLP) printing of microstructures for microfluidics applications based on a machine learning approach. *Virtual Phys. Prototyp.* 19 (1), e2318774. <https://doi.org/10.1080/17452759.2024.2318774>.
- Werner, J.G., Rodríguez-Calero, G.G., Abruna, H.D., Wiesner, U., 2018. Block copolymer derived 3-D interpenetrating multifunctional gyroidal nanohybrids for electrical energy storage. *Energy Environ. Sci.* 11 (5), 1261–1270. <https://doi.org/10.1039/C7EE03571C>.
- Xi, H., Zhou, Z., Zhang, H., Huang, S., Xiao, H., 2023. Multi-morphology TPMS structures with multi-stage yield stress platform and multi-level energy absorption: design, manufacturing, and mechanical properties. *Eng. Struct.* 294, 116733. <https://doi.org/10.1016/j.engstruct.2023.116733>.
- Xing, Z., Yong, H., 2021. Nonlinear dynamic behaviors and PID control of viscoelastic dielectric elastomer balloons. *J. Intell. Mater. Syst. Struct.* 33 (11), 1449–1464. <https://doi.org/10.1177/1045389X211057214>.
- Yuan, P., et al., 2024. Horizontally-oriented barium titanate@polydome/polyimide nanocomposite films for high-temperature energy storage. *J. Colloid Interface Sci.* 662, 1052–1062. <https://doi.org/10.1016/j.jcis.2024.02.109>.
- Zhang, J., et al., 2020. Improving actuation strain and breakdown strength of dielectric elastomers using core-shell structured CNT-Al2O3. *Compos. Sci. Technol.* 200, 108393. <https://doi.org/10.1016/j.compscitech.2020.108393>.
- Zhang, X.-Y., Liu, Y., Chen, X., Li, Z., Su, C.-Y., 2023. Adaptive Pseudoinverse control for constrained Hysteretic nonlinear systems and its application on dielectric elastomer actuator. *IEEE ASME Trans. Mechatron.* 1–13. <https://doi.org/10.1109/TMECH.2022.3231263>.
- Zhou, J., Hong, W., Zhao, X., Zhang, Z., Suo, Z., 2008. Propagation of instability in dielectric elastomers. *Int J Solids Struct* 45 (13), 3739–3750. <https://doi.org/10.1016/j.ijsolstr.2007.09.031>.